Structure sensitivity of nitrogen–doped carbon–supported metal catalysts in dihalomethane hydrodehalogenation

Ali J. Saadun [a,1], Andrea Ruiz–Ferrando [b,1], Simon Büchele [a], Dario Faust Akl [a], Núria López [b,*], Javier Pérez–Ramírez [a,*]

[a] Institute for Chemical and Bioengineering, Department of Chemistry and Applied Biosciences, ETH Zurich, Vladimir-Prelog-Weg 1, 8093 Zürich, Switzerland
[b] Institute of Chemical Research of Catalonia (ICIQ), The Barcelona Institute of Science and Technology, Av. Països Catalans 16, 43007 Tarragona, Spain

ARTICLE INFO

ABSTRACT

Nanostructuring metal catalysts has been demonstrated as an attractive strategy to enable selective hydrodehalogenation of CH_2X_2 (X = Cl, Br) to CH_3X, but active phase size effects of promising metals and the role of the halogen are still poorly understood. Herein, the impact of these parameters on performance (activity, selectivity, and stability) is systematically assessed by employing a platform of N–doped carbon–supported metal nanostructures (Ir, Pt, Ru, and Ni), ranging from single atoms (SA) with defined coordination environment to nanoparticles (NP) of *ca.* 3.0 nm. Catalytic tests reveal that when compared to single atoms, highest reaction rates are attained over NP–based systems, which also exhibit improved stability ranking as Ir ≈ Pt > Ru ≫ Ni, independent of the halogen. The product distribution was markedly affected by the nanostructure and speciation of the active center as well as the dihalomethane type. Specifically, CH_3Cl is the main reaction product over SA in hydrodechlorination, achieving an exceptional selectivity over Ir (up to 95%). In contrast, NP mainly generated CH_4 or coke. Comparable patterns were observed in hydrodebromination, except over Ru, which exhibited an inverse structure–selectivity trend. Density Functional Theory simulations shed light on the speciation of the active phase and identified the adsorption and dissociation energies of CH_2X_2 and H_2 as descriptors for catalytic reactivity. These findings elucidate hydrodehalogenation performance patterns, highlighting the impact of nanostructuring and the halogen type to advance future catalyst design.

1. Introduction

The development of innovative heterogeneous catalysts with enhanced performance and prolonged lifetimes takes a prominent place to tackle global environmental issues whilst meeting increasing demands for commodity chemicals [1,2]. Significant advances have been made in engineering well–defined materials with versatile architectures at the nanoscale [3,4], thereby overcoming structural nonuniformity that hinders the identification of active sites and the correlation of relationships at the molecular level [5]. Among several examples, single–atom catalysts, containing spatially isolated metal atoms on appropriate hosts, have attracted significant attention in recent years [6–9]. These systems have proven effective for the derivation of structure–performance trends in various chemical transformations [10,11], such as hydrochlorina-

tion [12,13] or alkynes semi-hydrogenation [14,15]. Specifically, isolated atoms displayed distinct characteristics with respect to the conventional supported nanoparticles [16,17]. Therefore, a systematic investigation of the nanostructure using a platform of catalysts ranging from single atoms with defined environments up to nanoparticles with controlled size, on catalytic performance constitutes an important step for the rational design of promising systems [18].

An application of potential practical relevance is the halogen–mediated natural gas upgrading to chemicals and fuels through hydrodehalogenation of dihalomethanes (CH_2X_2, X = Cl, Br) [19,20]. Selectively reforming these polyhalogenated compounds is required since they contribute to halogen and carbon–losses in the downstream halomethanes (CH_3X) upgrading step [21,22]. Various nanoparticle–based metal catalysts (Fe, Co, Ni, Cu, Ru, Rh, Ag, Ir, Pt) deposited on SiO_2 were studied in CH_2Br_2 hydrodebromination (HDB), revealing an outstanding CH_3Br selectivity over ruthenium (≤96%), great propensity to CH_4 over iridium and platinum (>50%), intermediate selectivity performance of nickel and rhodium (<60%), and inactive behavior of the other metals

(Fe, Co, Cu, and Ag) [23]. Despite its selective character, Ru/SiO$_2$ deactivated rapidly due to coking and sintering, whereas the iridium and platinum nanoparticles displayed the highest activity and stability. A global performance descriptor based on the adsorption strength of the halogen/carbon fragment on the active metal phase was presented to rationalize the observed reactivity patterns [23]. Building on these results, a recent study systematically investigated nuclearity– and host effects, using a platform of activated– (AC) and nitrogen–doped (NC) carbon–supported platinum nanostructures, from single atoms to nanoparticles of *ca.* 4 nm, in CH$_2$Br$_2$ hydrodebromination. The exceptional CH$_3$Br selectivity over the NC–supported single atoms (≤98%) was disclosed, outperforming AC–supported analogues and the reference catalyst Ru/SiO$_2$. The performance was explained by the geometric effects of the single atom and the participation of nitrogen sites in the reaction by storage of H–atoms [24].

In contrast to HDB, only a single study targeted selective CH$_2$Cl$_2$ hydrodechlorination (HDC) to CH$_3$Cl [25]. Therein, SiO$_2$–supported ruthenium, platinum, and iridium nanoparticles were investigated, showing a low selectivity to CH$_3$Cl (≤38% with CH$_4$ as main pro-

duct, achieved over Ir/SiO$_2$). Attempts to increase the selectivity by supporting Ir nanoparticles (0.8–1.6 nm) on ZrO$_2$, Al$_2$O$_3$, CeO$_2$, anatase TiO$_2$, and MgO did not provide the desired improvements. On the other hand, epitaxially directed iridium nanostructures on rutile TiO$_2$ showed unprecedented activity and CH$_3$Cl selectivity (≤95%), though limited lifetime due to poisoning by chlorination. Other relevant iridium nanostructures, such as single atoms, were not evaluated which hampers the formulation of robust structure–performance relationships. Furthermore, current CH$_2$X$_2$ HDH studies were confined to a single halogen, leaving ample room for further investigations [23].

To systematically address the catalytic search, we synthesized a platform of Ir/NC catalysts with distinct nanostructures, ranging from single atoms to size–controlled nanoparticles of *ca.* 3.5 nm, and assessed their performance in both HDC and HDB. By extending the scope to other NC–supported metals (Pt, Ru, and Ni) prepared as single atoms and nanoparticles (Fig. 1), we consistently investigate active phase size– and halogen effects with the aim to advance the design of promising hydrodehalogenation catalysts.
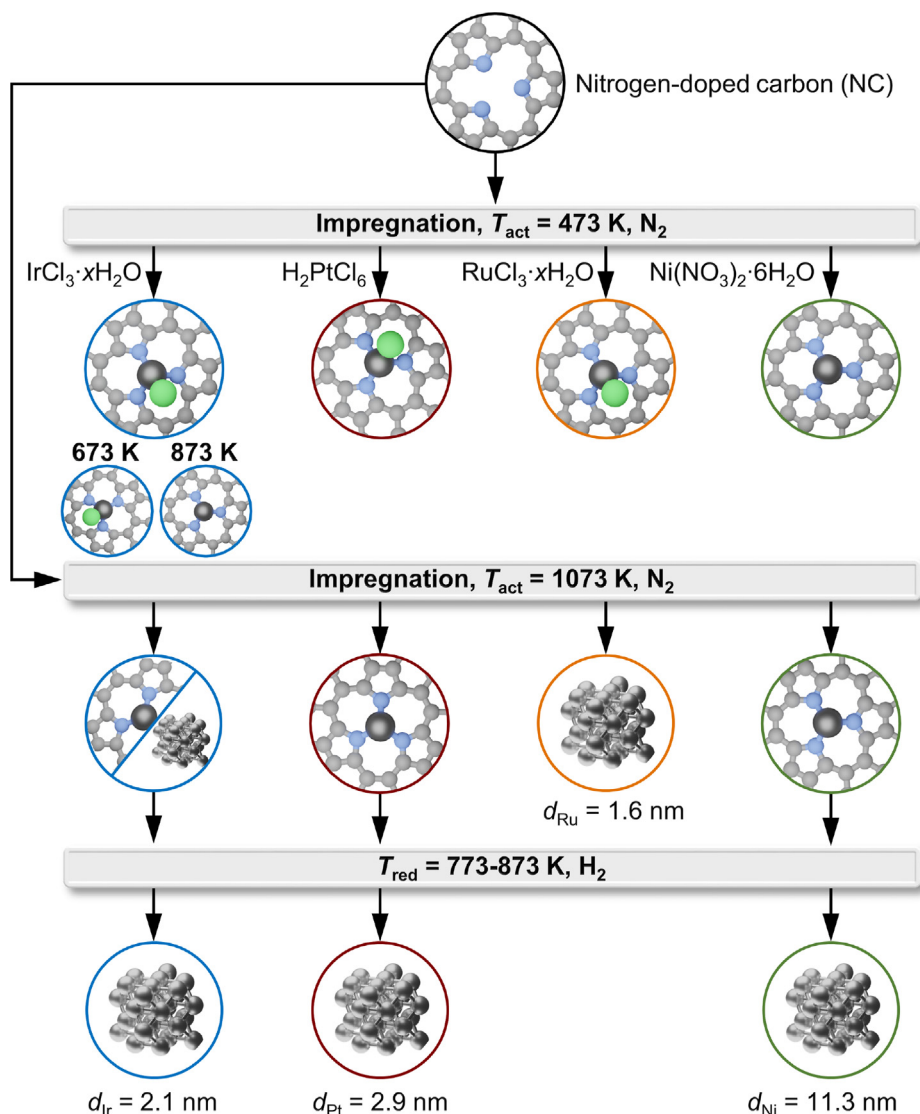

Fig. 1. Schematic representation of the NC–supported metal catalysts developed in this study. Color code: N, blue; C, light grey; Cl, green; metal, dark grey. (For interpretation of the references to color in this figure legend, the reader is referred to the web version of this article.)

2. Experimental

2.1. Catalyst preparation

Commercially available AC (Norit ROX 0.8) was used for evaluating the catalytic response of this metal–free support. NC was synthesized following the protocol reported by Kaiser *et al.*[12] Prior to its use as carrier for metal species, the NC was ground and sieved into particles of 0.4–0.6 mm. The metal precursors, $IrCl_3 \cdot xH_2O$ (abcr, 99.9%), H_2PtCl_6 (abcr, 99.9%), $RuCl_3 \cdot xH_2O$ (abcr, 99.9%), and $Ni(NO_3)_2 \cdot 6H_2O$ (Strem Chemicals, 99.9%) were dispersed on the support *via* incipient wetness impregnation. Appropriate amounts of the precursors required to obtain a nominal metal loading of 1 wt% were fully dissolved in a volume of deionized water (Pt and Ni) or aqua regia (Ir and Ru) equal to the pore volume of the carrier. The precursor solution was added dropwise to the support, and the resulting mixture was magnetically stirred for 2 h at room temperature. The impregnated solids were dried at 473 K for 16 h in static air (heating rate = 5 K min^{-1}). Subsequently, all samples were thermally activated (T_{act} = 473–1073 K) for 16 h in N_2 atmosphere (heating rate = 5 K min^{-1}). The catalysts were referred to as $M/NC–T_{act}$, where M denotes the metal (Ir, Pt, Ru, and Ni). The Ir/NC–1073, Pt/NC–1073, and Ni/NC–1073 catalysts underwent an additional reductive treatment in 20 vol% H_2/He (PanGas, purity 5.0) flow for 3 h at elevated temperatures (T_{red} = 773 or 873 K, heating rate = 10 K min^{-1}) and are denoted as Ir/NC(773), Pt/NC(873), and Ni/NC(773). Fig. 1 provides a guideline for the catalysts developed in this study.

2.2. Catalyst characterization

Powder X–ray diffraction (XRD) was measured in a PANalytical X'Pert PRO–MPD diffractometer with Bragg-Brentano geometry by applying Ni–filtered Cu Kα radiation (λ = 1.54060 Å). The data were recorded in the 10–70° 2θ range with an angular step size of 0.017° and a counting time of 0.26 s per step. N_2 sorption at 77 K was measured in a Micromeritics TriStar II analyzer. The samples (*ca.* 0.10 g) were degassed to 50 mbar at 423 K for 12 h prior to the measurement. The Brunauer–Emmett–Teller (BET) method was applied to calculate the total surface area, S_{BET}. The pore volume, V_{pore}, was determined from the amount of N_2 adsorbed at a relative pressure of p/p_0 = 0.98. The metal content in the catalysts was determined by inductively coupled plasma optical emission spectroscopy (ICP–OES) using a Horiba Ultima 2 instrument equipped with photomultiplier tube detection. The solids were dissolved in a HNO_3:H_2O_2 = 3:1 mixture under sonication until the absence of visible solids. CO pulse chemisorption was performed on a Thermo TPDRO 1100 set-up equipped with a thermal conductivity detector. Prior to the analyses, the samples (*ca.* 0.15 g) were pretreated at 423 K under flowing He (20 cm^3 STP min^{-1}) for 30 min, and reduced at 623 K under flowing 5 vol% H_2/He (20 cm^3 STP min^{-1}) for 30 min. Thereafter, 0.344 cm^3 of 1 vol% CO/He were pulsed over the catalyst bed every 4 min at 308 K until the area of the pulses remained constant. To avoid desorption of CO, the interval between successive pulses was minimized. Scanning transmission electron micrographs with a high-angle annular dark-field detector (HAADF–STEM) were acquired on FEI Talos and Hitachi HD2700CS microscopes operated at 200 kV. All samples were dispersed onto lacey carbon coated copper or nickel grids. The size distribution of the metal nanostructures was obtained by examining over 100 nanoparticles. X-ray photoelectron spectroscopy (XPS) measurements were performed on a Physical Electronics Quantera SXM X–ray instrument using monochromatic Al Kα radiation, generated from an electron beam operated at 15 kV, and equipped with a hemispherical capacitor electron-energy analyzer. The samples were analyzed at constant analyzer pass energy of 55.00 eV. The spectrometer was calibrated for the Au $4f_{7/2}$ signal at 84.0 ± 0.1 e V. The envelopes were fitted by mixed Gaussian–Lorentzian component profiles after Shirley background subtraction. The selected peak positions of the different species were based on literature reported data [26]. X-ray absorption fine structure (XAFS) measurements at the (Ir, Pt) L_2 and L_3- and (Ru) K–edge were carried out at the SuperXAS beamline. The incident photon beam provided by a 2.9 T superbend magnet was selected by a Si(111) channel-cut Quick-EXAFS monochromator. The rejection of higher harmonics and focusing were achieved with rhodium-coated collimating and toroidal mirrors, respectively, at 2.5 mrad. The area of sample illuminated by the X-ray beam was 0.5 mm × 0.2 mm. All spectra were recorded in transmission mode at room temperature. The extended X-ray absorption fine structure (EXAFS) spectra were acquired with a 1 Hz frequency (0.5 s per spectrum) and then averaged over 15 min. The procedures for analysis and fitting of the EXAFS spectra are reported elsewhere [12,27].

2.3. Catalyst evaluation

The hydrodechlorination of CH_2Cl_2 (HDC) and hydrodebromination of CH_2Br_2 (HDB) were conducted at ambient pressure in a home–made continuous–flow fixed–bed reactor set-up. H_2 (Pan-Gas, purity 5.0), He (carrier gas, PanGas, purity 5.0), and Ar (internal standard, PanGas, purity 5.0) were dosed by a set of digital mass flow controllers (Bronkhorst) and the liquids, CH_2Br_2 (Acros Organics, 99%) or CH_2Cl_2 (Sigma Aldrich, >99.9%), were fed by a syringe pump (Fusion 100, Chemyx) equipped with a water-cooled syringe to a vaporizer unit operated at 393 (CH_2Br_2) or 353 K (CH_2Cl_2). A quartz reactor (internal diameter, d_i = 12 mm) was loaded with the catalyst or metal–free carrier (catalyst/carrier weight, W_{cat} = 0.05–1 g, particle size, d_p = 0.4–0.6 mm) and heated to the reaction temperature (T = 523 K) in an electrical oven under He flow. The catalyst bed was allowed to stabilize for at least 10 min before the reaction mixture was fed at a total volumetric flow of F_T = 30 and 50 cm^3 STP min^{-1} for HDB and HDC, respectively, and with a composition of CH_2X_2:H_2:Ar:He = 6:24:5:65 (vol%, X = Cl, Br). The kinetic tests were performed with a variable feed composition of CH_2X_2:H_2:Ar:He = 6:6–72:5:17–83. Downstream linings were heated at 393 K to prevent the condensation of unconverted reactants and/or products. Carbon-containing compounds (CH_2X_2, CH_3X, CH_4) and Ar were quantified online *via* a gas chromatograph equipped with a GS–Carbon PLOT column coupled to a mass spectrometer (GC–MS, Agilent GC 6890, Agilent MSD 5973 N). After GC–MS analysis, the gas stream was passed through two impinging bottles in a series containing an aqueous solution of NaOH (1 M) for neutralization prior to its release in the ventilation system.

The conversion of the reactant, $X(CH_2X_2)$, was calculated using Eq. (1),

$$X(CH_2X_2) = \frac{n(CH_2X_2)_{in} - n(CH_2X_2)_{out}}{n(CH_2X_2)_{in}} \times 100, \% \qquad (1)$$

where $n(CH_2X_2)_{in}$ and $n(CH_2X_2)_{out}$ are the molar flows of CH_2Br_2 or CH_2Cl_2 at the reactor inlet and outlet, respectively. The selectivity, S (j), to product j (j: CH_3X, CH_4) was calculated according to Eq. (2),

$$S(j) = \frac{n(j)_{out}}{n(CH_2X_2)_{in} - n(CH_2X_2)_{out}} \times 100, \% \qquad (2)$$

where $n(j)_{out}$ is the molar flow of product j at the reactor outlet. The selectivity to coke, S_{coke}, in all tests was calculated according to eq. (3), which is based on a generally applied carbon balance that determines the accumulation of carbon–containing species in the catalyst.

Table 1
Characterization data of the catalysts.

Catalyst	d_M[a]/nm	M content[b]/wt%	S_{BET}[c]/m^2 g^{-1}			V_{pore}[d]/cm^3 g^{-1}		
			Fresh	HDC[e]	HDB[e]	Fresh	HDC[e]	HDB[e]
Ir/NC-473	SA	0.98	274	204	–	0.23	0.20	–
Ir/NC-673	SA	0.96	310	170	–	0.26	0.22	–
Ir/NC-873	SA	1.01	411	230	59	0.33	0.24	0.12
Ir/NC-1073	1.3	0.99	370	109	–	0.30	0.18	–
Ir/NC(773)	2.1	0.98	379	106	74	0.31	0.17	0.16
Pt/NC-1073	SA	0.94	363	182	30	0.32	0.20	0.10
Pt/NC(873)	2.9	1.00	545	189	215	0.43	0.27	0.22
Ru/NC-473	SA	1.08	400	207	37	0.32	0.24	0.12
Ru/NC-1073	1.6	0.97	324	133	31	0.27	0.18	0.12
Ni/NC-1073	SA	1.00	405	–	–	0.34	–	–
Ni/NC(773)	11.3	1.03	349	–	–	0.30	–	–

[a] : SA: single atoms.
[b] : ICP–OES.
[c] : BET model.
[d] : Volume of N$_2$ adsorbed at p/p_0 = 0.98.
[e] : Used in CH$_2$Cl$_2$ hydrodechlorination (HDC) or CH$_2$Br$_2$ hydrodebromination (HDB). Reaction conditions as specified in the captions of Figs. 2 and 8.

$$S_{coke} = \frac{n(CH_2X_2)_{in} - n(CH_2X_2)_{out} - n(j)_{out}}{n(CH_2X_2)_{in}} \times 100, \% \quad (3)$$

Therein, $n(CH_2X_2)_{in}$, $n(CH_2X_2)_{out}$, and $n(j)_{out}$ stand for the molar in– and outlet flows of gaseous reactants and products. The reaction rate, r, based on the metal loading and expressed with respect to the consumption of CH$_2$X$_2$, was calculated using **eq.** (4),

$$r = \frac{n(CH_2X_2)_{in} \times X(CH_2X_2)}{W_{cat} \times \omega_M} \text{ , mol}_{CH_2X_2} \text{ h}^{-1} \text{ mol}_M^{-1} \quad (4)$$

where W_{cat} is the weight of the catalyst and ω_M is the metal loading determined by ICP–OES analysis (Table 1). The turnover frequency, *TOF*, was calculated using **eq.** (5),

$$TOF = \frac{n(CH_2X_2)_{in} \times X(CH_2X_2)}{W_{cat} \times \omega_M \times D_M} \text{ , h}^{-1} \quad (5)$$

where D_M is the metal dispersion, determined by CO pulse chemisorption. A metal dispersion of 100% was used for the single atom–based catalysts. After the tests, the reactor was quenched to room temperature in He flow, and the catalyst was retrieved for further characterization analyses. Evaluation of the dimensionless moduli based on the criteria of Carberry, Mears, and Weisz–Prater [28,29] indicated that the catalytic tests were performed in the absence of mass and heat transfer limitations.

2.4. Computational details

Density Functional Theory (DFT) on models of the nanoparticles and single atoms representing the different catalytic systems was employed as implemented in the Vienna ab–initio Simulation Package (VASP 5.4.4) [30,31]. Generalized Gradient Approximation with the Perdew–Burke–Ernzerhof functional (GGA–PBE) [32] was used to obtain the exchange–correlation energies with dispersion contributions introduced via Grimme's DFT–D3 approach [33]. Projector Augmented Wave (PAW) [34,35] and plane waves with a cut-off energy of 450 eV, with spin polarization allowed when needed, were chosen to represent the inner electrons and the valence monoelectronic states, respectively. For simulations of the single atoms, a one-layer (6 × 6) slab of graphitic carbon separated by 19 Å of vacuum was used and sampled through a gamma–centred grid of 3 × 3 × 1 k–point grid. Carbon materials are ill–defined for several reasons: (i) the graphene layers constituting them can be stacked in different arrangements due to the van der Waals interactions; (ii) they store different types of struc-

tural and particularly point defects; (iii) depending on the atmosphere under which they are prepared they can have a variable (almost continuous) stoichiometry with different types of functionalities; (iv) overall if doped or created by different precursors a wider chemical versatile (and defect types) renders an almost continuous of chemical environments. This wide spread cannot be addressed efficiently by present characterization techniques to set structure–activity relationships as, for instance, EXAFS is not able to distinguish C/N/O coordination and vibrational patterns can hint on the nature of N-cavities. The computational solution to this conundrum is to devise a set of models compatible with the stoichiometry and nature of the most-abundant cavities according to the available characterization. In line with this, the NC support was represented by a set of three defects containing various nitrogen functionalities, including pyrrolic and/or pyridinic moieties, and different coordination structures; (i) non-planar 3 N and square-planar 4 N arrangements, labelled 3 × N5 (tri–pyrrolic), (ii) 4 × N6 (tetra-pyridinic), (iii) and 2 × N5 + 2 × N6 (tetra-pyrrolic/pyridinic), whereas AC was modelled by adding an epoxide on the carbon matrix, all adopted from previous studies [12]. Single atom catalysts were modelled by placing the metal atom in the centre of each cavity. For nanoparticles, systems were modelled as a four–layer p(3x3)–(1 1 1) fcc (Pt, Ir, and Ni), or a p(3x3)–(0001) hcp slab (Ru) interspaced along the z–direction by a vacuum space of 15 Å, and k-point sampling of 5 × 5 × 1 (Gamma centered). The two top layers and the adsorbates were allowed to relax while the bottom two were fixed to the bulk lattice. The arising dipole was corrected in all slab models [36]. Gas-phase molecules were optimized in a box of 14.0 × 14.5 × 15.0 Å^3. For all investigated systems, structures were relaxed using convergence criteria of 10^{-4} eV and 10^{-5} eV for the ionic and electronic steps, respectively.

To assess the stability of the single atoms in the NC cavities, formation energies were estimated using the metal species and the scaffold as reference states. Binding energies of the halogen to the halogenated single atoms were calculated using the non-halogenated single atom and Br$_2$/Cl$_2$ as reference states. For the Gibbs free energy on the reaction network, CH$_2$X$_2$, H$_2$, and metal surfaces or pristine single atoms (defined as the isolated and non–chlorinated metal species) were utilized, and the vibrational, rotational, and translational entropic contributions from gas–phase reactant molecules were included.

The Climbing Image Elastic Band (CI–NEB) method [37,38], improved dimer method [39,40] and quasi–Newton algorithms

were employed to locate the transition states (TS) in the reaction profiles, where the TS were further verified by their single imaginary frequency character.

All the structures presented in this work have been uploaded to the ioChem–BD database [41] https://iochem-bd.iciq.es/browse/review-collection/100/29816/440d6583bf1645c23bc615b4 [42].

3. Results and discussion

3.1. Hydrodehalogenation over Ir/NC catalysts

To build a fully consistent platform on NC supports and since iridium has been targeted as a potential HDX active phase our work starts with the preparation of NC–supported iridium catalysts, applying the reported procedures, which include dry impregnation of the chloride precursor on NC followed by thermal activation to obtain the final catalyst, designated Ir/NC–T_{act} (T_{act}, 473–1073 K). This procedure follows our recent synthetic strategies presenting structures of platinum and ruthenium (1 wt% metal basis) on NC, from (chlorinated) single atoms to nanoparticles [24,27].

In the low– and medium–temperature catalysts, Ir/NC–473, 673, and 873, the metal was mostly atomically dispersed as evident from the HAADF–STEM images (Fig. 2) and corroborated by the absence of iridium diffraction peaks in the XRD patterns (Fig. S1). The high–temperature system, Ir/NC–1073, contains nanoparticles with an average size of 1.3 nm, although single atoms still make up a considerable fraction of the nanostructures. Aimed at further sintering the active phase, an additional reduction step in an H₂–rich atmosphere at 773 K was applied to Ir/NC–1073. The resulting Ir/NC(773) exhibited a narrow nanoparticle size distribution with an average size of 2.1 nm (Fig. 2), in agreement with its XRD pattern that shows diffraction peaks compatible with the metallic phase. Although nanoparticles are dominant in Ir/NC (773), the presence of single atoms cannot be totally discarded. Further analysis of the Ir/NC catalysts by N₂–sorption revealed the close similarity of the specific surface areas (S_{BET}, 310–392 m² g⁻¹) and pore volumes (V_{pore}, 0.23–0.32 cm³ g⁻¹), whereas ICP–OES confirmed that the metal content was approximately the targeted 1 wt% (Table 1). The speciation of the nitrogen content was preserved over the whole temperature range, as indicated by N 1 s XPS analysis (**Table S1**). Fitting the Ir 4f spectra of the Ir/NC–473, 673, and 873 samples revealed dominant contributions at binding energies (BEs) of ca. 62.4 and 63.0 eV commonly assigned to oxidized species (Fig. 3, **Fig. S2**) [25,43], corroborating the atomic dispersion of iridium as visualized by HAADF–STEM. In contrast, the main feature of the Ir/NC–1073 and Ir/NC(773) samples was centered at ca. 61.0 eV, compatible with the metallic phase [43]. Notably, analysis of the Cl 2p XPS suggests that the nature of the iridium site in the single–atom based catalysts is directly affected by the activation temperature (**Fig. S2**). In particular, Ir/NC–873 shows no peaks that could be ascribed to Cl–species, suggesting that the iridium single atom is only coordinated to N/O–related cavities in the scaffold, whereas the low–temperate catalyst reveal contributions at 198.0 and 200.2 eV, indicative of the presence chlorinated species [44]. This evolution is in line with previous reports that documented the gradual change of the coordination environment of platinum single atom from predominant Cl– to N/O–neighboring atoms at higher activation temperatures [12,24]. As anticipated, chlorine was not detected in the nanoparticle–based (NP–based) catalysts, Ir/NC–1073 and Ir/NC (773).

The catalytic performance of the derived iridium nanostructures was evaluated in HDC and HDB, which were conducted at constant reaction temperature (523 K), feed composition (CH₂X₂:

H₂:Ar:He = 6:24:5:65), and atmospheric pressure. The initial HDC activity, expressed per surface iridium atom (*TOF*), decreases in the following order (Fig. 4a): Ir/NC(773) ≫ Ir/NC–1073 > Ir/NC–873 > Ir/NC–673 ≈ Ir/NC–473. Nanoparticles display a higher activity than their chlorinated SA–based analogues (>5 times), showing comparable performance to benchmark rutile TiO₂–supported iridium (Ir/r–TiO₂, **Table S2**). Moreover, single atoms with a N/O coordination (Ir/NC–873) exhibit up to 2.5–fold higher *TOF* than their chlorinated counterparts, possibly due to the ability of the metal center to activate the reactants. Assessment of the product distribution at ca. 20% CH₂Cl₂ conversion (Fig. 4a), revealed that Ir/NC–873 yields a high CH₃Cl selectivity (≤95%), matching that of Ir/r–TiO₂. A key feature that governs this performance is the absence of coordinating chlorine atoms, which mainly promote coking pathways (**Fig. S3**).

Upon increasing the active phase size from single atoms to nanoparticles of 2.1 nm, the selectivity to CH₃Cl decreases to ca. 48% at the expense of the generation of CH₄. The Ir/NC–1073 system, with an average nanoparticle size of 1.3 nm, exhibits a relatively high CH₃Cl selectivity (ca. 70%), which is due to the considerable number of single atoms still present. The activity– and selectivity trends were complemented with stability tests, revealing that all systems deactivate over time. The stability decreases in the following order: Ir/NC(773) > Ir/NC–1073 > Ir/NC–873 > Ir/NC–673 > Ir/NC–473 (**Fig. S4**), thus showing that NP–based systems display improved stability compared to their SA–based counterparts (up to ca. 4 times higher activity after 10 h, **Table S2**). Despite these results, Ir/r–TiO₂ remains the best performing catalyst, showing unparalleled reactivity and stability in HDC (**Table S2**). Nevertheless, the fixed structure directed by the epitaxial growth of iridium on rutile–type carriers does not allow investigations on active phase size effects, which is one of the main aims of this study.

Further, the NC–supported iridium nanostructures were also tested in HDB to determine possible halogen effects (Fig. 4b). Notably, the activity was comparable to that in HDC, indicating that the type of halogen plays a minimal role. The selectivity to CH₃Br shows a comparable volcano shape as to that of CH₃Cl, with the N/O–coordinated single atom system presenting the highest selectivity (>90%) regardless of the halogen. The increasing propensity to coke and CH₄ in chlorinated single atoms (<43%) and NP–based systems (<25%), respectively, are also observed, albeit less pronounced than in HDC (**Fig. S3**). To provide a complete overview of halogen effects, HDB stability tests were conducted. The deactivation patterns were comparable to that in HDC (**Fig. S4**), with nanoparticles preserving their initial activity better than single atoms.

Briefly, the results identify that the initial HDH reactivity of iridium catalysts is predominantly governed by their active phase nanostructure: irrespective of the choice of halogen, nanoparticles display the highest activity and stability, and chlorine–free single atoms exhibit superior selectivity to CH₃X compared to their Cl–coordinated counterparts and nanoparticles, which favor coke and CH₄ production, respectively.

3.2. Hydrodehalogenation over Pt, Ru, and Ni nanostructures

This study was further expanded with nanostructures of platinum and ruthenium (Fig. 1), which were chosen as representative metals based on previous HDH studies and prepared following established synthesis procedures [12,27]. Furthermore, nickel–based catalysts were also included in the evaluation, despite that their HDH performance is considered poor [23]. Previous investigations revealed that moderate changes in the adsorption energies of the CH/Br fragments could lead to a dramatic increase in the HDB
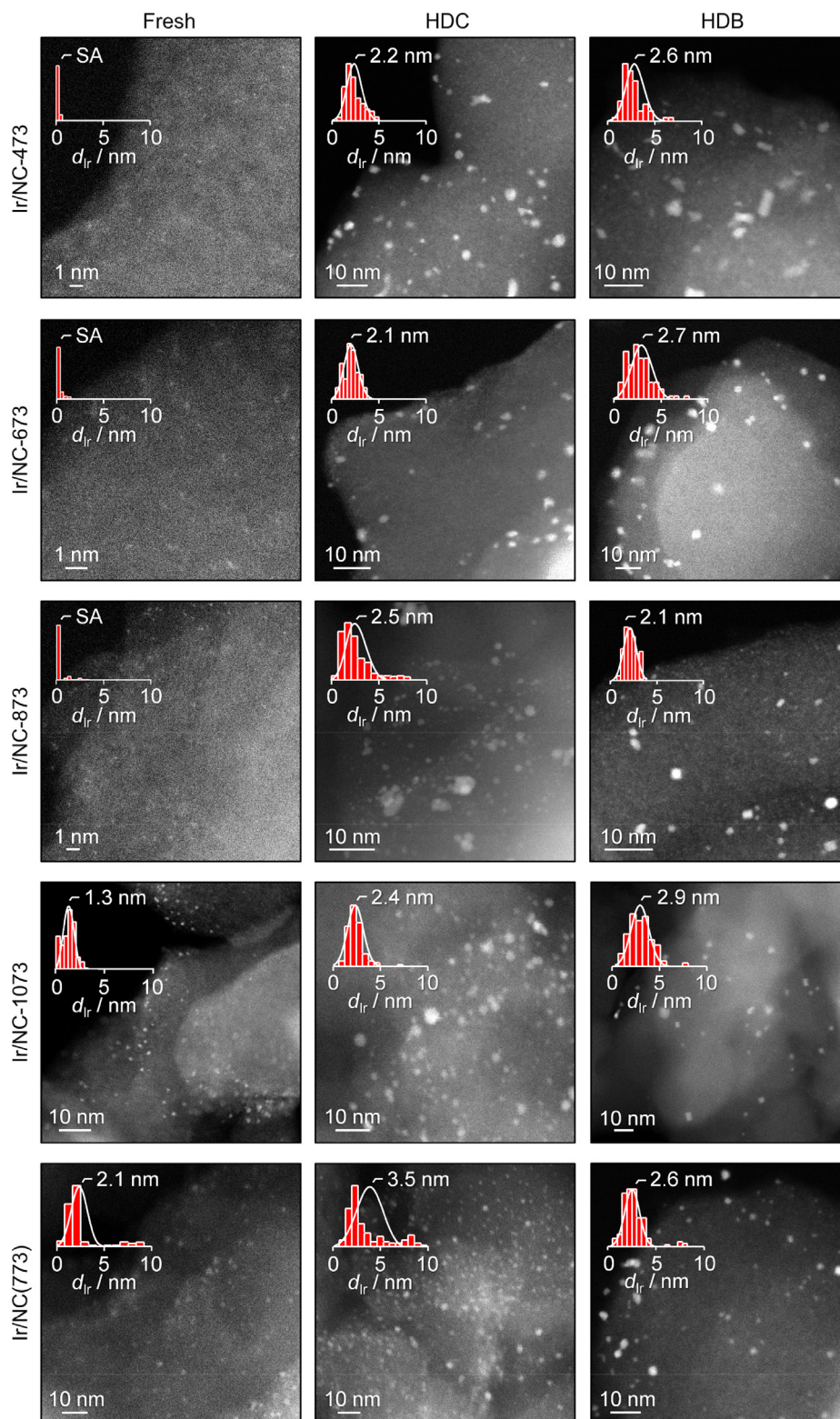
Fig. 2. HAADF-STEM micrographs with particle size distributions (inset, SA: single atoms) of the iridium-based catalysts in fresh form and after 10 h in CH_2Cl_2 hydrodechlorination (HDC) or CH_2Br_2 hydrodebromination (HDB). Reaction conditions: F_T/W_{cat} = 100–300 cm^3 min^{-1} g$_{cat}^{-1}$ in HDC and 150–400 cm^3 min^{-1} g$_{cat}^{-1}$ in HDB. All catalysts were evaluated at CH_2X_2:H_2:Ar:He = 6:24:5:65 (X = Cl, Br), T = 523 K, and P = 1 bar.

selectivity of nickel, rendering it an attractive candidate for studying nuclearity– and halogen effects [23].

To achieve the targeted metal speciation (one system based on single atoms and one on nanoparticles, Fig. 1), each system was prepared applying a thermal treatment step (under N_2 atmo-

sphere) at a specific temperature (T_{act}), indicated as M/NC–T_{act}. Systems that underwent an additional reduction step under H_2 at elevated temperatures (T_{red}) with the aim to induce sintering of the metal were labelled M/NC(T_{red}). The resulting six catalysts were denoted Pt/NC–1073, Pt/NC(873), Ru/NC–473, Ru/NC–1073,
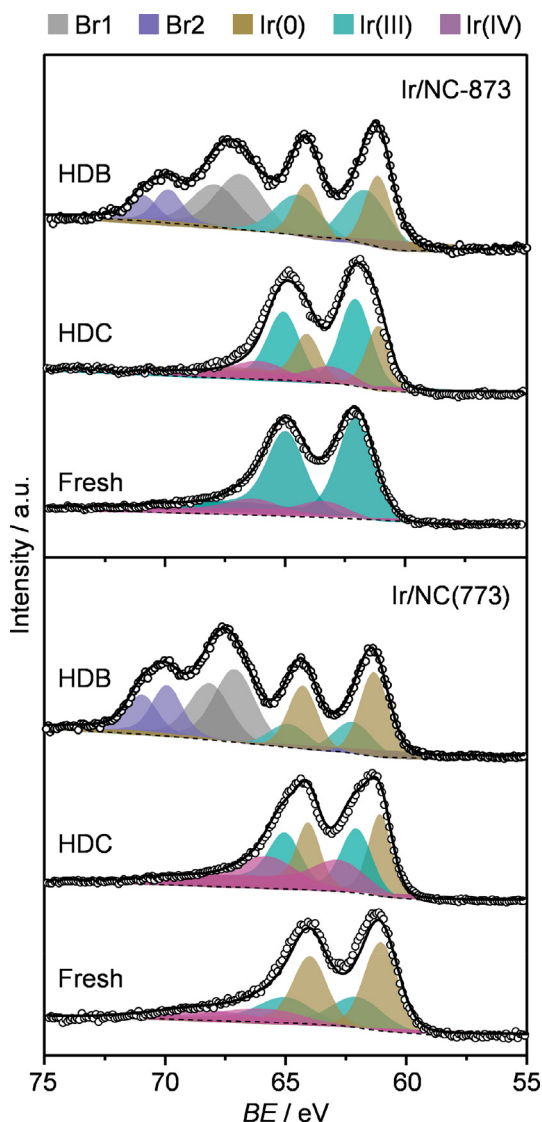
Fig. 3. Ir 4*f* XPS spectra of selected iridium-based catalysts in fresh form and after 10 h in CH₂Cl₂ hydrodechlorination (HDC) or CH₂Br₂ hydrodebromination (HDB). Black lines and open circles represent the overall fit and the raw data, respectively, while the colored areas indicate the fit of distinct chemical components. Reaction conditions as specified in the caption of Fig. 2.

Fig. 4. a) Turnover frequency (*TOF*) and the selectivity to CH₃X (X = Cl, Br) in **a)** CH₂Cl₂ hydrodechlorination (HDC) and **b)** CH₂Br₂ hydrodebromination (HDB) over the iridium-based catalysts. The *TOF* was assessed at a constant space velocity of 200 cm³ min⁻¹ g$_{cat}^{-1}$ and *tos* = 15 min, while the CH₃X selectivity was determined at ca. 20% CH₂X₂ conversion achieved by adjusting the space velocity in the range of F_T:W_{cat} = 100–300 cm³ min⁻¹ g$_{cat}^{-1}$ in HDC and 150–400 cm³ min⁻¹ g$_{cat}^{-1}$ in HDB. Other reaction conditions: CH₂X₂:H₂:Ar:He = 6:24:5:65, *T* = 523 K, and *P* = 1 bar, and *tos* = 15 min.

Ni/NC(773), indicate that active phase sintering occurred, leading to an average nanoparticles size of *ca.* 11.3 nm, in agreement with the XRD patterns that show a sharp reflection of metallic nickel. Interestingly, the necessary synthesis conditions to obtain nanoparticles are different across the metals: at 1073 K, iridium and ruthenium have an average nanoparticle size of 1.3 and 1.6 nm, respectively. At that temperature, platinum and nickel are still atomically dispersed, suggesting that these metals are highly stabilized in the cavities of the host as demonstrated by modeling, see below.

To gain insights on the chemical state of the metals, XPS analysis was conducted. In accordance with the micrographs, a metallic phase was absent in the SA-based ruthenium and platinum catalysts, Ru/NC-473 and Pt/NC-1073 (Fig. 6). The Ru 3*d* spectrum of Ru/NC-473 revealed a contribution at a binding energy of *ca.* 464.1 eV (Fig. 6a), commonly assigned to RuCl₃ [27,45], suggesting that these single atoms are coordinated to chlorine. On the other hand, the dominant feature of the Pt 4*f* spectrum of Pt/NC-1073 is centred at *ca.* 73.0 eV, indicating the oxidized character of the platinum atoms (Fig. 6b) [26,46]. In line with the XPS results, the EXAFS analysis shows pronounced Cl– and N/O–coordination for the ruthenium and platinum single atoms, respectively (Fig. 7).

Ni/NC–1073, and Ni/NC(773) (for an overview, please consult Table 1).

The data revealed that the porous properties of the catalysts are comparable with the iridium–based systems, exhibiting S_{BET} and V_{pore} in the range of 324–545 m² g⁻¹ and 0.27–0.43 cm³ g⁻¹, respectively; whereas ICP–OES confirmed that the actual metal content was close to the nominal value of 1 wt% (Table 1). The HAADF–STEM images clearly visualize the attainment of single atoms in Ru/NC–473 and Pt/NC–1073 (Fig. 5), and corroborated by XRD analysis, where reflections assigned to the metallic phases are not observed (**Fig. S5**). The micrographs further show that nanoparticles are the dominating nanostructure in the high–temperature catalysts, Ru/NC–1073 and Pt/NC(873), with average particle size of 1.6 and 2.9 nm, respectively (Fig. 5). Similar to platinum, the high–temperature nickel catalyst (Ni/NC–1073) still exhibits single atoms as main species (**Fig. S6**), thus requiring an additional high-temperature reduction step for the evolution of nickel into nanoparticles. The micrographs of the resulting catalyst,
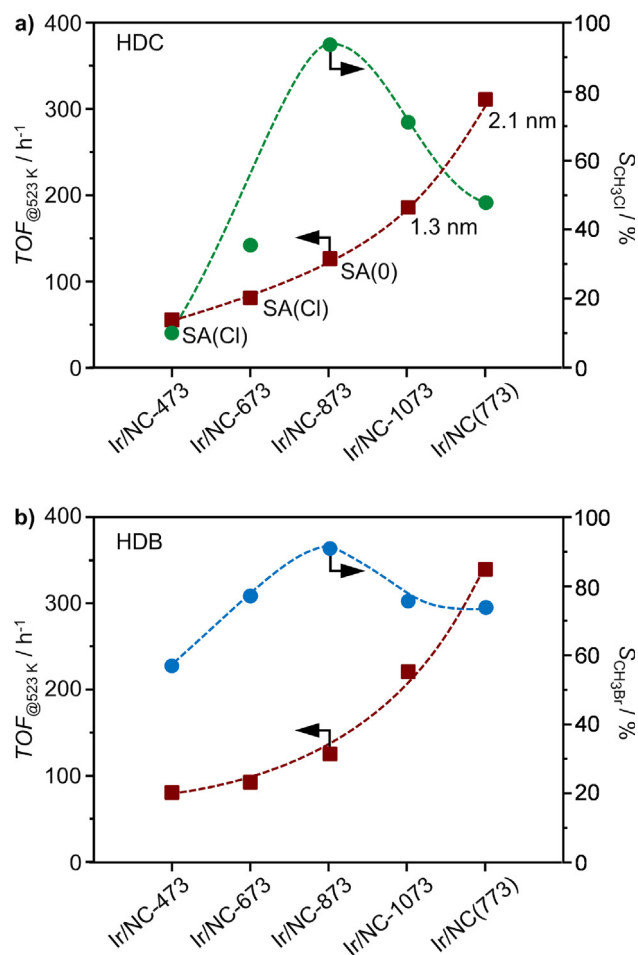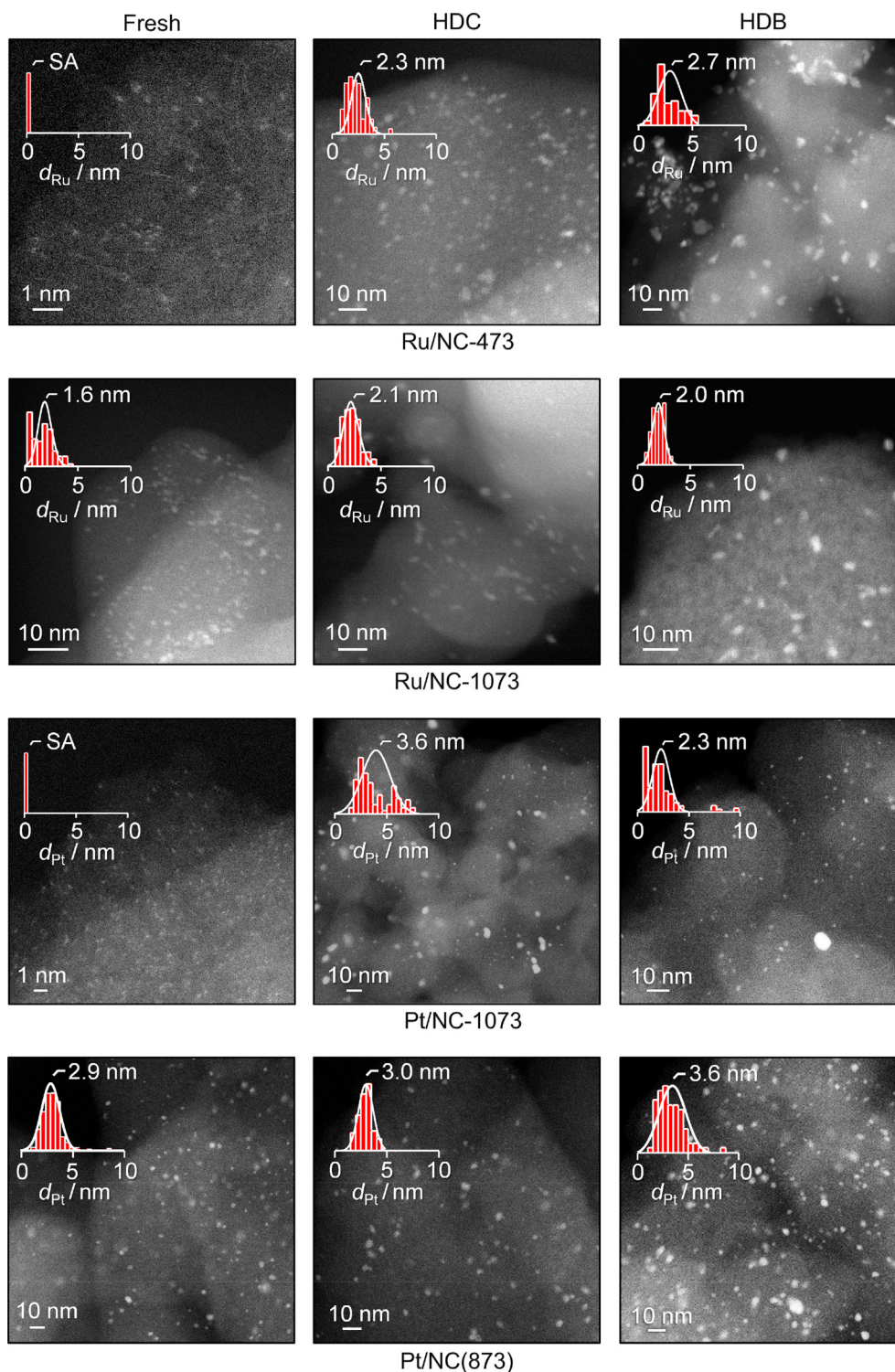
Fig. 5. HAADF–STEM micrographs with particle size distributions (inset, SA: single atoms) of selected catalysts in fresh form and after 10 h in CH_2Cl_2 hydrodechlorination (HDC) or CH_2Br_2 hydrodebromination (HDB). Reaction conditions as specified in the caption of Fig. 2.

However, a clear N/O–Ru signal is also present, implying that a fraction of ruthenium single atoms are also N/O–coordinated.

The performance of the platinum–, ruthenium–, and nickel–based catalysts was evaluated in HDC as well as in HDB at 573 K. For comparative purposes, representative iridium SA– and NP–based catalysts were selected (Ir/NC–873 and Ir/NC(773), respectively) and included in Fig. 8. Analysis of the HDC results revealed the following trend of decreasing metal activity with the speciation

of the dominating species indicated between brackets (Fig. 8a): Ir (NP) $\approx$ Pt (NP) > Ir (SA) $\approx$ Pt (SA) > Ru (NP) > Ru (SA) > Ni (NP) > Ni (SA), with the nickel–based systems being virtually inactive. Over each metal, nanoparticles provide higher activity than the single atom analogues, which is in line with the trend previously distinguished over iridium–based catalysts (Fig. 4). A similar pattern was observed in HDB (Fig. 8b), implying that halogen effects on catalytic activity are minimal, irrespective of the metal.
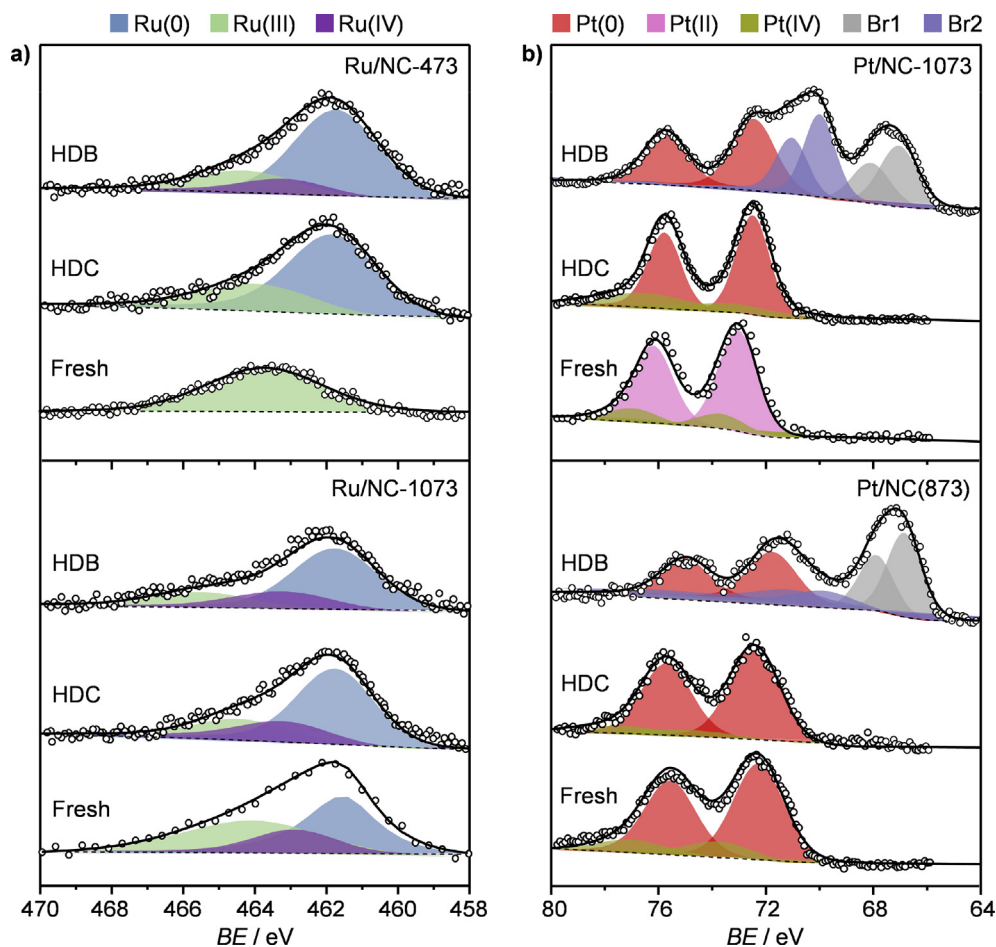
Fig. 6. a) Ru 3*d* and b) Pt 4*f* XPS spectra of selected catalysts in fresh form and after 10 h in CH$_2$Cl$_2$ hydrodechlorination (HDC) or CH$_2$Br$_2$ hydrodebromination (HDB). Black lines and open circles represent the overall fit and the raw data, respectively, while the colored areas indicate the fit of distinct chemical components. Reaction conditions as specified in the caption of Fig. 2.
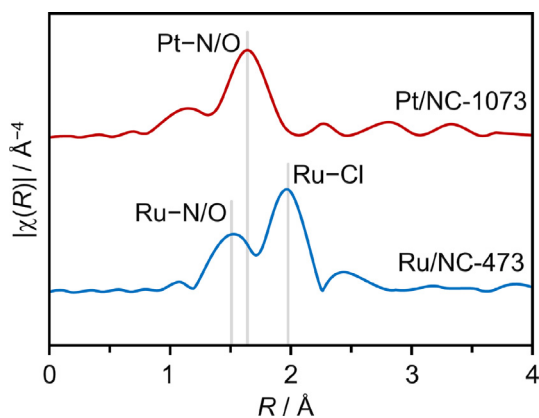

Fig. 7. Ru L_3 and Pt L_3 EXAFS spectra of selected catalysts in fresh form.

In contrast, the selective behavior of the catalyst depends on both nuclearity and the type of halogen. In HDC, SA–based systems display a CH$_3$Cl selectivity of *ca.* 95% (Ir), 80% (Pt), and 70% (Ru), higher than the NP–based catalysts (Fig. 8**a**). Nanoparticles provided a lower selectivity (≤50%), favoring CH$_4$ (Ir and Pt, up to 46%) and coke (Ru and particularly Ni, up to 92%).

These results are comparable with the selectivity patterns obtained in HDB (Fig. 8**b**), although iridium and platinum nanoparticles are less prone to over hydrogenation (CH$_4$ selectivity up to *ca.*

30%). In stark contrast, ruthenium nanoparticles display a higher propensity to CH$_3$Br (≤94%) than their single atom counterparts (≤71%). In addition, whereas ruthenium nanoparticles coke significantly in HDC (up to 60%), this side reaction does not occur in HDB as evidenced by the only two products CH$_3$Br and CH$_4$. The performance of ruthenium breaks with the trend that single atoms are more selective to the monohalogenated product, as seen in HDC.

Stability tests were also conducted to gain a complete overview of the catalytic performance. The depletion of activity was expressed with the constant k_D to enable a direct comparison, indicating the activity loss per hour derived *via* linear regression of the data in the time–on–stream (*tos*) range of 0.25–10 h (**Fig. S7**). The active phase nanostructure clearly affects catalyst lifetime, with nanoparticles preserving their initial activity better than single atoms in HDC and HDB (Fig. 8**c, d**). The stability decreases in the following order for both reactions: Pt (NP) > Ir (NP) > Ir (SA) ≈ Pt (SA) ≈ Ru (NP) > Ru (SA). Evolution of the products are presented in **Fig. S7**, revealing that SA–based systems, except for ruthenium which shows an opposite trend, display enhanced propensity to CH$_4$ over time. This suggests that sintering of the active phase into nanoparticles occurred during exposure to the reaction conditions.

In summary, NC-supported metal (Ir, Pt, Ru, and Ni) catalysts with single atoms or nanoparticles as dominating nanostructure were prepared, characterized, and tested in HDC and HDB. It was revealed that hydrodehalogenation activity and stability are enhanced over nanoparticles when compared to single atoms, whereas the latter limit over hydrogenation and coking pathways,
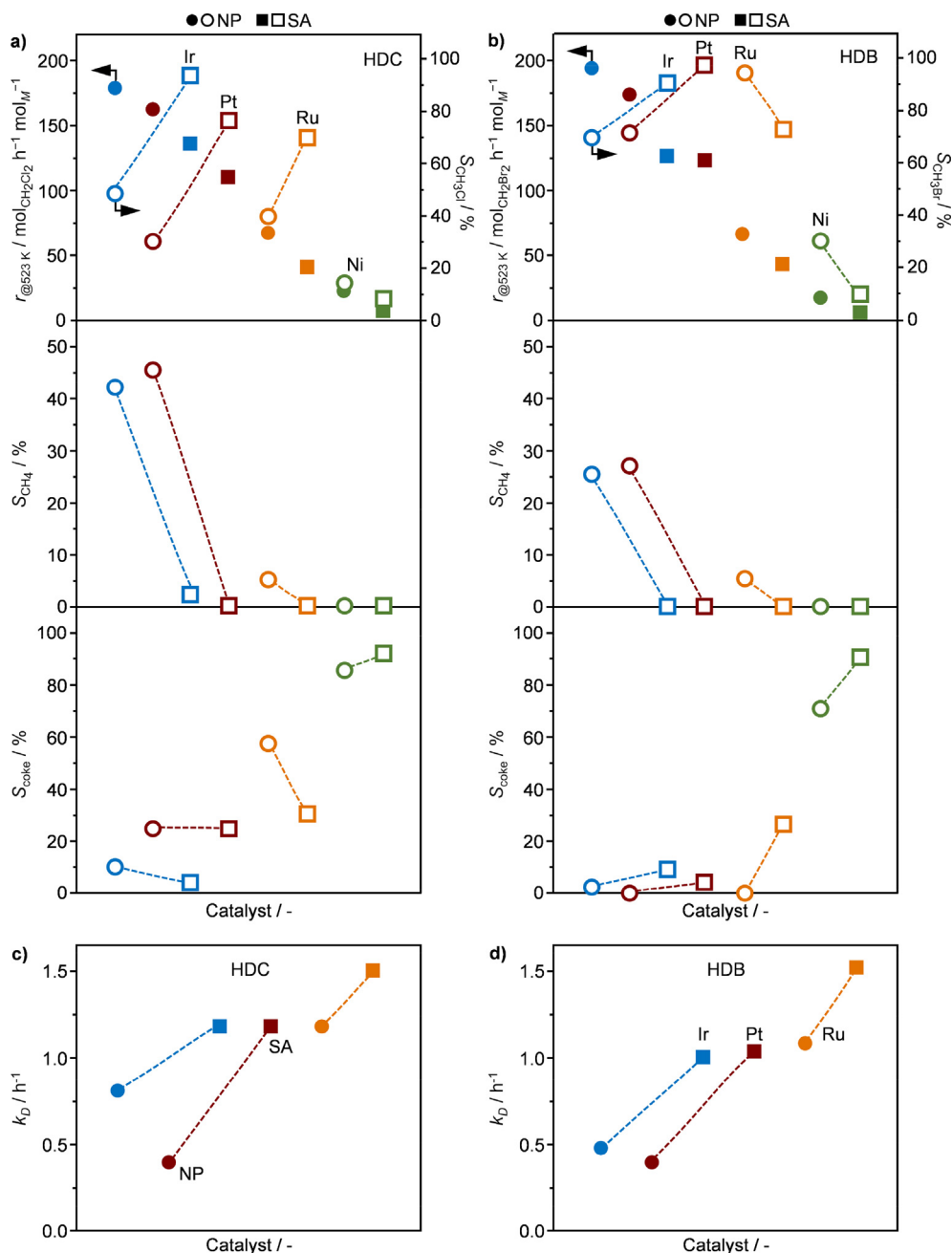
Fig. 8. Rate of CH_2X_2 (X = Cl, Br) hydrodehalogenation and product selectivity in **a)** CH_2Cl_2 hydrodechlorination (HDC) and **b)** CH_2Br_2 hydrodebromination (HDB) over selected catalysts. The deactivation constants (k_D) as a function of the metal and speciation in **c)** HDC and **d)** HDB. The rates were assessed at a constant space velocity of 200 cm³ min⁻¹ g$_{cat}^{-1}$, while product selectivities were determined at ca. 20% CH_2X_2 conversion achieved by adjusting the space velocity in the range of F_T:W_{cat} = 50–300 cm³ min⁻¹ g$_{cat}^{-1}$ in **a)** and 30–400 cm³ min⁻¹ g$_{cat}^{-1}$ in **b)**. Other reaction conditions: CH_2X_2:H_2:Ar:He = 6:24:5:65, T = 523 K, P = 1 bar, and *tos* = 15 min. SA and NP stand for single atoms and nanoparticles, respectively. The dotted lines serve as eye trackers.

leading to outstanding CH_3X selectivity. Ruthenium displays an inverse trend due to halogen effects, showing a higher selectivity to CH_3Br over nanoparticles. Nevertheless, all catalysts deactivate over time and further investigation of the used systems is required to gain insight on deactivation mechanisms.

3.3. Kinetic analysis and deactivation mechanisms

Kinetic experiments reveal significant differences in the partial order of H_2 over the catalysts, which can be grouped as systems (*i*) selective to CH_3X, showing a $p(H_2)$ in the range of 0.41–0.58, (*ii*) that display significant selectivity to CH_4 with $p(H_2)$ of 0.78–0.91,

and (*iii*) that predominantly produce coke (Ru nanoparticles in HDC), showing a partial order of 0.67 (Fig. 9). Particularly single atoms are in the first group, whereas platinum and iridium nanoparticles are in the second. Notably, all nanoparticles have a higher $p(H_2)$ than their single atom analogues in both HDC and HDB except for ruthenium in HDB, which exhibits a $p(H_2)$ of 0.55 for single atoms and 0.43 for nanoparticles. These fingerprints suggest that the reaction mechanism may differ over the nanostructures and depends on the type of halogen. The results are likely a direct consequence of the ability to activate H_2 and store H–atoms that can react with surface species, which may depend on the geometry of the active phase and participation of the basic sites
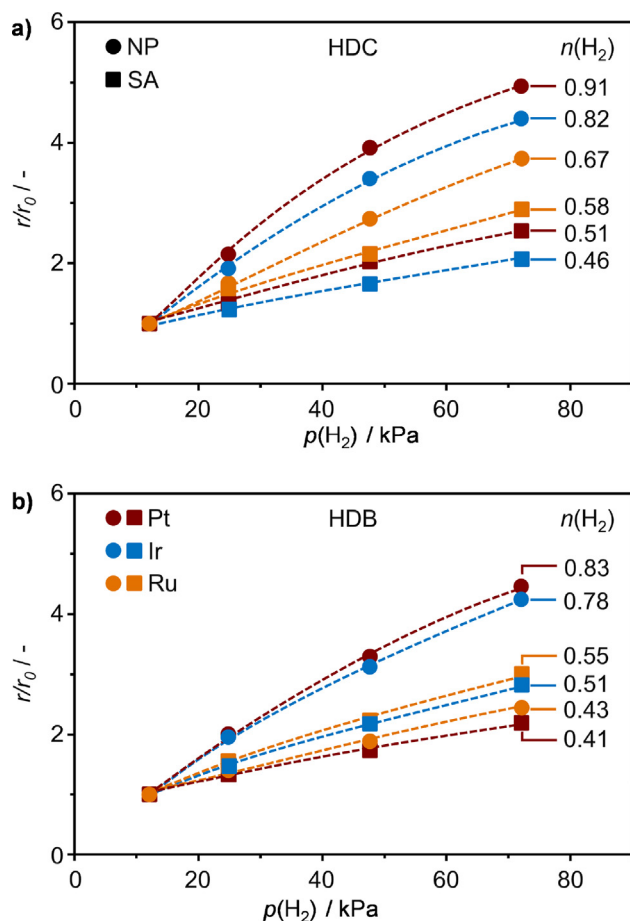
Fig. 9. Rate of **a)** CH_2Cl_2 hydrodechlorination (HDC) and **b)** CH_2Br_2 hydrodebromination (HDB) of selected catalysts as a function of the inlet partial pressure of H_2. Each catalytic data point was gathered using materials in fresh form to exclude the possible influence of catalyst deactivation. Reaction conditions: CH_2X_2:H_2:Ar: He = 6:12–72:5:17–77 (X = Cl, Br), F_T/W_{cat} = 50–750 cm³ min⁻¹ g$_{cat}^{-1}$ in **a)** and 100–800 cm³ min⁻¹ g$_{cat}^{-1}$ in **b)**, T = 523 K, P = 1 bar, and *tos* = 15 min.

with XRD analysis (**Fig. S1**), showing reflections compatible with metallic iridium, and by the XPS spectra that display contributions assigned to the metallic phase (Fig. 3, **Fig. S2**). Furthermore, the peaks at BEs of 67.4 and 70.0 eV reveal the poisoning of the surface via bromination in HDB (Fig. 3) [24], whereas chlorination occurs in HDC as evidenced by the contributions at 197.9 and 200.8 eV (**Fig. S2**). This indicates that all iridium–based catalysts, in addition to fouling due to the deposition of carbonaceous species and active phase sintering, also suffer from halogenation.

Whereas all active systems, regardless of the metal, suffer from the poor stability of the carrier, used ruthenium and platinum catalysts were characterized to assess the extent of metal sintering and halogenation on their lifetime. Similar to their iridium counterparts, HAADF–STEM microscopy reveals that ruthenium– and platinum single atoms undergo pronounced sintering, increasing up to 2.7 and 3.6 nm, respectively, whereas nanoparticles remain relatively stable (Fig. 5). The weak reflections assigned to the metallic phase in the XRD spectra of the used platinum catalysts and Ru/NC–1073 suggest that larger nanoparticles were formed. This observation was confirmed by XPS analysis, distinguishing contributions at BEs of 461.8 (Ru/NC–473) and 72.1 eV (Pt/NC–1073), representing metallic ruthenium and platinum, respectively (Fig. 6). Further analysis of the spectra indicates that surface chlorination is limited over both metals, displaying a relatively unaltered fraction of oxidized species in used ruthenium–based systems compared to the fresh one, whereas platinum catalysts are largely metallic. On the other hand, the catalysts used in HDB display contributions assigned to Br–species (Fig. 6, **Fig. S8**), suggesting bromination of the surface. However, as platinum is mostly in the zero-oxidation state, it suffers the least from halogenation, which implies that mainly the carrier was brominated.

In short, the loss of catalytic performance over time–on–stream is caused by: (*i*) fouling by coking, which is expected to occur over all systems due to carrier metastability, (*ii*) active phase sintering, more pronounced for single atoms, and (*iii*) halogenation. While chlorination mainly occurs on iridium–based systems, bromine poisons iridium, ruthenium, and platinum catalysts, albeit the latter to a lesser extent. Overall, these results underline that deactivation mechanisms are complex and intertwined, governed by three modes that depend on the type of halogen, the metal, and its nuclearity, thereby highlighting the need for individual optimization strategies to develop stable systems.

3.4. Speciation analysis

Whereas Ir/NC activated at 1073 K results in an average nanoparticle size of 1.3 nm (Fig. 2), the platinum– and nickel–based systems that underwent a similar thermal treatment (Pt/NC–1073 and Ni/NC–1073) have single atoms as predominant species (Fig. 5, **Fig. S6**). Furthermore, the platinum single atoms are non–chlorinated, in contrast to the single atoms in Ru/NC–473, Ir/NC–473, and Ir/NC–673 (Fig. 5, Fig. 6), which are coordinated to Cl. These results suggest that the speciation, as nanoparticle or as (chlorinated) single atom, depends on various factors, including the anchoring sites in the NC carrier, the metal, and the activation temperature. Therefore, to complement the characterization of the materials, a molecular–level understanding of the active phase speciation can help establishing more robust structure–performance relationships. For this purpose, Density Functional Theory (DFT) studies were conducted. Therein, the NC support was represented by a set of three defects; (*i*) non-planar 3 N and square-planar 4 N arrangements, labelled 3 × N5 (tri-pyrrolic), (*ii*) 4 × N6 (tetra-pyridinic), (*iii*) and 2 × N5 + 2 × N6 (tetra-pyrrolic/pyridinic) [12]. Formation energies were evaluated to shed light on the interaction of the single atom with the host, using

of the carrier in the reaction, as was found in previous HDB studies [24].

To examine the development of the iridium–based catalysts during exposure to HDC and HDB conditions, selected systems were characterized after 10 h on–stream using N_2–sorption, XRD, HAADF STEM, and XPS, revealing three main deactivation mechanisms: (*i*) fouling due to coking, (*ii*) metal sintering, and (*iii*) poisoning by halogenation. HAADF–STEM micrographs of the used systems display the sintering of single atoms into nanoparticles with an average size in the range of 2.1–2.7 nm, regardless of the halogen type (Fig. 2). Even though the nanoparticle size of these catalysts is comparable after 10 h on–stream, their performance is dissimilar due to the contributions of coking and surface halogenation. Analysis of the structural properties point at the remarkable instability of the NC carrier (Table 1), with the specific surface areas (S_{BET}) and pore volumes (V_{pore}) strongly decreasing after exposure to the reaction conditions (up to 90 and 70% lower than the original values, respectively). This suggests that deposition of carbonaceous species on the active sites contributes significantly to activity losses over all catalysts, likely more pronounced over catalysts that generate coke as main product, such as Ir/NC–473, Ir/NC–673 (**Fig. S3**). On the other hand, the NP–based iridium catalyst, (Ir/NC(773)), was less prone to active phase agglomeration with an increase of the particle size from 2.1 to 3.5 and 2.6 nm in HDC and HDB, respectively. These results were corroborated
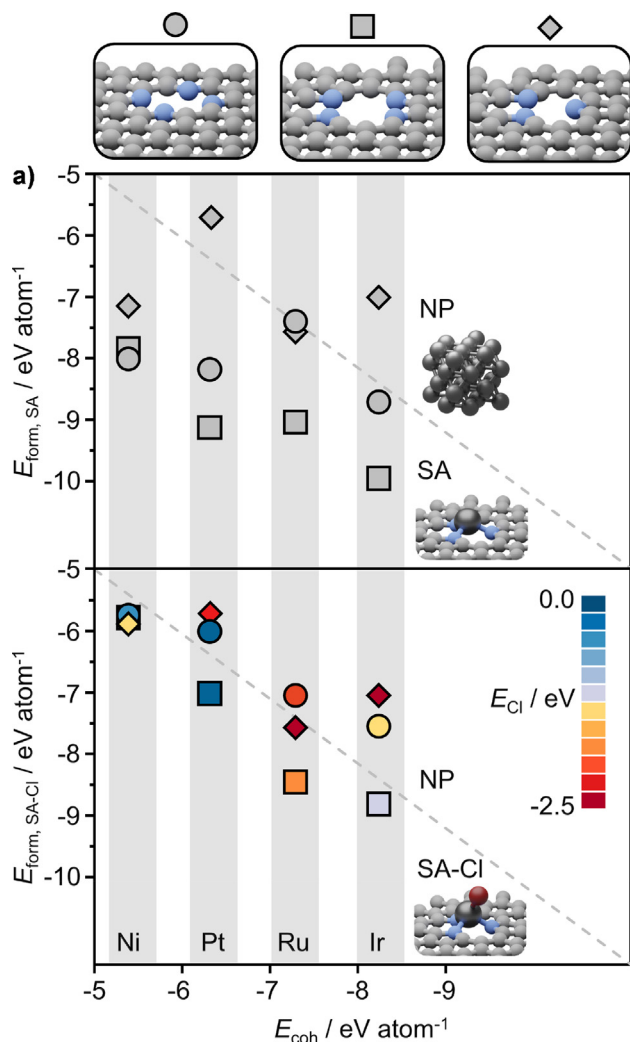
Fig. 10. Formation energies of pristine (top panel) and chlorinated (bottom panel) single atom catalysts as a function of the the cohesive energy. The shapes of the data points represent the N-defects (top), whereas their interior color refers to the chlorine affinity (warm for strong affinity, cold for weak binding). Dashed lines represent values where $E_{coh} = E_{SA}$, at which the energy to form single atoms (SA) or nanoparticles (NP) would be equal.

metal chloride precursors MCl (M = Ir, Pt, Ru, or Ni), the pristine metal species (M), and the NC support as reference states.

The results of the speciation analysis reveal two general trends related to the Cl–ligands and cavities in the NC–carrier (Fig. 10, **Table S3**):

(i) starting from the pristine single atom, iridium and ruthenium display the highest affinity toward chlorination, with binding energies ranging from –1.13 to –2.44 eV, explaining why these systems remain chlorinated at elevated temperatures, and

(ii) single atoms in 3 × N5 sites are expected to be more chlorinated than those in the 4 × N6 and 2 × N5 + 2 × N6 cavities due to the square–planar arrangement in 4 N-defects, which is responsible for the superior atom stabilization. This prevents the sintering of single atoms into nanoparticles during the removal of Cl at increasingly higher activation temperatures.

To further understand the speciation trends, cohesive energies were computed. Ruthenium and iridium present the strongest

propensity to leaching, with cohesive energies of –7.3 and – 8.0 eV/atom, respectively (Fig. 10), whereas nickel (–5.3 eV/atom) and platinum (-6.2 eV/atom) display lower values. These results are in agreement with the experimentally observed metal speciation, which showed that nickel and platinum remained as single atoms while iridium and ruthenium were mainly nanoparticles at 1073 K (Figs. 2 and 5, **Fig. S6**). Consequently, the stabilization of iridium and ruthenium single atoms in N–containing defects is not sufficient to prevent their sintering at elevated temperatures, while nickel and platinum single atoms exhibit superior stability in most cavities. To further assess the effect of N–functionalities on the atomic dispersion on the carrier, adsorption energies of single atoms on a N–free carrier were evaluated. Previous investigations disclosed the synthesis of platinum single atoms on activated carbon (AC) [12,24]. Nonetheless, the significantly smaller adsorption energy of the atoms in AC cavities (–3.15 eV, Table S3) relative to the anchoring sites in NC (<-5.44) indicate that the latter provide better stability. Comparable values were found for nickel (–3.97 and < –7.12 eV on AC and NC, respectively). In stark contrast, the atomic dispersion of iridium and ruthenium on AC is not favored due to the full coordination and high cohesive energy of these metals. This leads to insufficient atom anchoring on AC, thereby highlighting the positive impact of N–moieties on single atom stability. The potential catalytic activity of single atoms in each defect was studied by exploring the adsorption energy of the substrates, CH_2Cl_2 and CH_2Br_2. Metal single atoms in the tri–pyrrolic (3 × N5) cavity displayed superior substrate activation (**Table S4**), in line with previous studies [24] and in agreement with the presence of pyrrolic sites as shown in the characterization data (**Table S1**). Hence, a single atom in the 3 × N5 cavity was retained as the most representative for single atom–based catalysts.

3.5. Mechanistic studies

The reaction network leading to CH_3Br, CH_4 and C is described (**Table S5**) and the associated thermodynamic and kinetic parameters were calculated (**Tables S6-S8**). The Gibbs free energies were computed including entropic contributions from the molecules, using CH_2X_2, H_2, and the corresponding catalysts as reference systems operating at 523 K (**Fig. S9**, **Fig. S10**).

At first, the effect of a full coordination of the single atom with Cl ligands was assessed. The network starts by the dissociative adsorption of CH_2X_2 on the active ensembles, leading to CH_2X^*. The presence of Cl in the active phase hinders the activation of CH_2X_2 over the single atoms, with barriers ranging from 0.9 to 1.8 eV. Furthermore, subsequent adsorption of H_2 on CH_2X^* is virtually prohibitive as the valence of the metal atom is full. Consequently, chlorinated sites are prone to coke, which is consistent with the observed selectivity performance of chlorinated iridium single atoms (**Fig. S3**). In contrast to the chlorinated systems, the dissociation of CH_2X_2 on the pristine (non–chlorinated) single atoms is quite exothermic and instantly leads to CH_2X^* fragments. Nickel–based systems form an exception to that rule. The challenging activation of CH_2X_2 on the nickel single atoms (~2 eV) can be rationalized in terms of the low affinity toward both halogens, being *ca.* 1 eV lower compared to the iridium, platinum, and ruthenium single atoms (**Table S9**), resulting in poor catalytic activity in both HDC and HDB (Fig. 8).

Once the substrate is dissociated into CH_2X^*, one of the following steps take place: *(i)* heterolytic H_2 dissociation promoted by the basicity of the cavity [24] or *(ii)* halogen elimination to form CH_2^*, thereby filling the valence of the metal atom in an octahedral configuration, which poisons the active site by impeding the incorporation of H_2, thus promoting coke formation. Although this step is energetically feasible (<0.9 eV in all cases, except for Ni), the

greater stability of the CH_2X^* compared to the dissociated $CH_2^*+X^*$ inevitably lowers the population of $CH_2^*X^*$ intermediates, which promotes H_2 incorporation on CH_2X^*. Upon the heterolytic dissociation of H_2, HX^* and CH_3X^* are formed on the single atom, thereby re–establishing the active site after their desorption.

Among the three active single atom catalysts (Ir, Ru and Pt, Fig. 8), ruthenium displays the lowest activity and a significant selectivity to coke (~30%), owing to the presence of chlorinated sites in the active phase, thus following comparable performance patterns as the chlorinated iridium single atoms. In contrast, single atoms of iridium and platinum display superior activity and CH_3X selectivity performance due to their facile hydrogen dissociation (<1.10 eV, Fig. 11), and favourable CH_2X_2 adsorption (<0.6 eV).

The basic N–sites of the host can participate in the reaction by storing H–atoms that can be transferred to other moieties. This leaves the single atom free for coordination, thereby enhancing catalytic activity [24]. To further assess the contribution of N–functionalities to the reaction, dissociation energies of H_2 over single atoms on the carbon supports were computed. Hydrogen undergoes barrierless homolytic dissociation over platinum and nickel on AC (**Table S10**). In contrast, even though the reaction is energetically feasible, activation of H_2 over AC–supported iridium and ruthenium is not possible, as these single atoms cannot be stabilized (**Table S3**). To gain further insights, experimental evaluation of bare NC and AC in CH_2X_2 hydrodehalogenation (reaction conditions specified in the caption of Fig. 2) was conducted, revealing the inactivity of AC. On the other hand, NC displayed low activity (**Table S2**), suggesting that N–species can act as catalytically active sites. Nevertheless, the metal–free carrier deactivates rapidly, showing deactivation constants more than 6–fold higher than Pt/NC–1073 in both reactions. These results indicate that the catalytic response is mainly determined by the metal species in the cavity.

Still, the contribution of the host is crucial in enabling the adsorption of the substrates and the full mechanism. Particularly, the evolution of CH_2X^* moieties depends on the cooperation of the support with the single atom species, since it enables the formation of CH_3X by providing a sufficient number of protons and prevents the generation of CH_2^*, which likely leads to coke. High CH_3X selectivity is ensured over iridium and platinum due to the participation of the NC carrier. In addition to promoting the heterolytic dissociation of H_2, the diffusion of carbonaceous species and halogen fragments over the surface of the scaffold is hindered due to the non-continuous structural morphology of the host. Consequently, CH_4 is not generated and only coke is formed as a side product when H_2 cannot be incorporated to CH_2X^*. The active phase sintering occurs due to the formation of mobile fragments during the course of the reaction. Such moieties are obtained when substrates are adsorbed on single atoms with non-planar configurations. The binding energy of the single atom to the scaffold is lowered and the resulting metal complex is susceptible to diffusion.

The facile homolytic dissociation of H_2 over the surface of metal nanoparticles results in higher hydrogen coverages when compared to single atoms, explaining the superior activity of nanoparticle-based catalysts in the hydrogenation paths (**Table S4**). The reaction starts similar to that over their single atom counterparts, but the system is more prone to form CH_2^*, facilitated by the diffusion of halogen and methylene moieties over the surface [24], which in general (except for ruthenium in HDB) leads to CH_4 and C. However, if H^* is incorporated on CH_2X^*, CH_3X^* is generated and subsequently desorbed. After the formation of CH_2^*, one of the following steps takes place: (*i*) CH_2^* dissociation to CH^* and H^* promoted by the diffusion of H^* and the affinity of the metal toward CH^* or (*ii*) H^* incorporation to form CH_3^* and subsequently, CH_4.

Whereas metal surfaces of the nanoparticles are continuous, multiple adsorption/reaction events take place simultaneously. Particularly, the HDC and HDB reactions lead to CH_2^* with almost no barrier for cleaving the second C—X bond. Over hydrogenation occurs over iridium and platinum sites due to the greatly exothermic formation of H^* intermediates (Fig. 11), which leads to the formation of CH_4. On the other hand, the high affinity to carbonaceous fragments such as CH_2^*, CH^*, and C^* results in coke over nickel nanoparticles. Even the penetration of C into the metal lattice is exothermic (-0.8 eV, **Table S11**), which can contribute to rapid catalyst deactivation in both HDC and HDB.

Among the nanoparticles, ruthenium shows a notable performance trend in HDB, where nanoparticles are more selective to CH_3Br than the single atom analogues. In HDC, the controlled H_2 coverage, due to a less favourable H_2 dissociation, leads to the formation of coke. However, in HDB, the binding strength of CH_2Br_2 on the metal surface is optimal (−0.13 eV, 0.94 eV for CH_2Cl_2), resulting in the exceptional performance of the nanoparticles. This defines energetic regions where HDC and HDB take place with improved selectivity (Fig. 11). Optimal H_2 adsorption and CH_2X_2 binding energies were found to be between 0.25 and 1.25, and lower than 0.6 eV, respectively.

Altogether, the systematic study of the synthetic platform for two closely related reactions allowed us to widen the conceptual framework encompassing synthesis, characterization and understanding allowing us to establish robust structure (species)-performance patterns.

4. Conclusions

In this study, a strategy combining catalytic evaluation complemented with extensive characterization of a platform of NC–supported metal nanostructures (Ni, Ru, Ir, and Pt), from single atoms to nanoparticles of ca. 3 nm, coupled with kinetic analysis and density functional theory was adopted to systematically investigate to effects of the active phase and the halogen on activity, selectivity and stability in CH_2X_2 hydrodehalogenation. Substantial activity differences were observed over the nanostructures, attaining the highest reaction rates over NP–based systems, ranking as Ir ≈ Pt > Ru ≫ Ni independent of the halogen. Moreover, these systems preserve their initial activity better than their single atom analogues, which mainly suffer from sintering. The catalytic tests
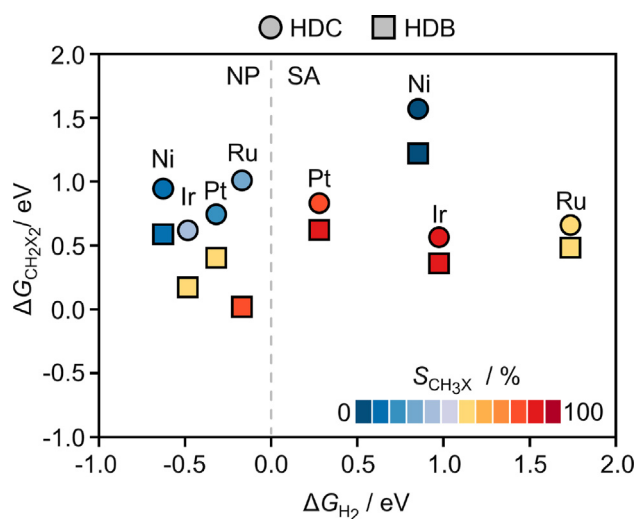

Fig. 11. Gibbs free adsorption energies of CH_2X_2 and H_2 over the nanoparticles (NP) and single atoms (SA). The interior color of the symbols indicates the selectivity to CH_3X obtained by the catalytic tests.

further revealed a marked impact of nuclearity, single atom coordination environment, and halogen type on the product distribution. In hydrodechlorination, CH_3Cl is the main reaction product over single atoms, whereas nanoparticles exhibited significant selectivity to CH_4 or coke. Among the metals, iridium–based single atoms exhibit exceptional CH_3Cl ($\leq 95\%$) selectivity, in stark contrast to their chlorinated analogues which favored the formation of coke (<90%). Comparable performance patterns were observed in hydrodebromination with the exception for ruthenium, which displayed an inverted selectivity–structure trend with improved CH_3Br selectivity over nanoparticles ($\leq 96\%$) compared to the single atoms ($\leq 72\%$). Kinetic and mechanistic studies correlate these results with the ability of the active phase to activate CH_2X_2 and H_2, and to store H–atoms. Furthermore, the intrinsic stability of the single atoms in the cavities and the potential catalytic response were computed, setting a basis for understanding the effects of synthetic protocols on speciation and coordination. The findings reported in this work are directed at elucidating hydrodehalogenation performance patterns, highlighting the impact of nanostructuring and the halogen type to advance future catalyst design.

Declaration of Competing Interest

The authors declare that they have no known competing financial interests or personal relationships that could have appeared to influence the work reported in this paper.

Acknowledgements

Appendix A. Supplementary material

Supplementary information associated with this article, containing additional characterization and catalytic data, can be found in the online version. The computed structures have been added to the ioChem-BD database ref. [42]. Supplementary data to this article can be found online at https://doi.org/10.1016/j.jcat.2021.10.008.

References

[1] R.A. Sheldon, Fundamentals of Green Chemistry: Efficiency in Reaction Design, Chem. Soc. Rev. 41 (4) (2012) 1437–1451, https://doi.org/10.1039/C1CS15219J.

[2] C.M. Friend, B. Xu, Heterogeneous Catalysis: a Central Science for a Sustainable Future, Acc. Chem. Res. 50 (3) (2017) 517–521, https://doi.org/10.1021/acs.accounts.6b00510.

[3] L. Liu, A. Corma, Metal Catalysts for Heterogeneous Catalysis: from Single Atoms to Nanoclusters and Nanoparticles, Chem. Rev. 118 (10) (2018) 4981–5079, https://doi.org/10.1021/acs.chemrev.7b00776.

[4] A.T. Bell, The Impact of Nanoscience on Heterogeneous Catalysis, Science 299 (5613) (2003) 1688–1691, https://doi.org/10.1126/science:1083671.

[5] X. Cui, Wu.u. Li, P. Ryabchuk, K. Junge, M. Beller, Bridging Homogeneous and Heterogeneous Catalysis by Heterogeneous Single-Metal-Site Catalysts, Nat. Catal. 1 (6) (2018) 385–397, https://doi.org/10.1038/s41929-018-0090-9.

[6] X.-F. Yang, A. Wang, B. Qiao, J. Li, J. Liu, T. Zhang, Single-Atom Catalysts: a new Frontier in Heterogeneous Catalysis, Acc. Chem. Res. 46 (8) (2013) 1740–1748, https://doi.org/10.1021/ar300361m.

[7] A. Wang, J. Li, T. Zhang, Heterogeneous Single-Atom Catalysis, Nat. Rev. Chem. 2 (6) (2018) 65–81, https://doi.org/10.1038/s41570-018-0010-1.

[8] J. Liu, Catalysis by Supported Single Metal Atoms, ACS Catal. 7 (1) (2017) 34–59, https://doi.org/10.1021/acscatal.6b01534.

[9] S.K. Kaiser, Z. Chen, D. Faust Akl, S. Mitchell, J. Pérez-Ramírez, Single-Atom Catalysts across the Periodic Table, Chem. Rev. 120 (21) (2020) 11703–11809, https://doi.org/10.1021/acs.chemrev.0c00576.

[10] F. Zhang, Y. Zhu, Q. Lin, L. Zhang, X. Zhang, H. Wang, Noble-metal Single-Atoms in Thermocatalysis, Electrocatalysis, and Photocatalysis, Energy Environ. Sci. 14 (5) (2021) 2954–3009, https://doi.org/10.1039/D1EE00247C.

[11] S. Mitchell, E. Vorobyeva, J. Pérez-Ramírez, The Multifaceted Reactivity of Single-Atom Heterogeneous Catalysts, Angew. Chem. Int. Ed. 57 (47) (2018) 15316–15329, https://doi.org/10.1002/anie.201806936.

[12] S.K. Kaiser, E. Fako, G. Manzocchi, F. Krumeich, R. Hauert, A.H. Clark, O.V. Safonova, N. López, J. Pérez-Ramírez, Nanostructuring unlocks high Performance of Platinum Single-Atom Catalysts for Stable Vinyl Chloride Production, Nat. Catal. 3 (4) (2020) 376–385, https://doi.org/10.1038/s41929-020-0431-3.

[13] G. Malta, S.A. Kondrat, S.J. Freakley, C.J. Davies, L.i. Lu, S. Dawson, A. Thetford, E.K. Gibson, D.J. Morgan, W. Jones, P.P. Wells, P. Johnston, C.R.A. Catlow, C.J. Kiely, G.J. Hutchings, Identification of Single-Site Gold Catalysis in Acetylene Hydrochlorination, Science 355 (6332) (2017) 1399–1403, https://doi.org/10.1126/science:aal3439.

[14] G. Vilé, D. Albani, N. Almora-Barrios, N. López, J. Pérez-Ramírez, Advances in the Design of Nanostructured Catalysts for Selective Hydrogenation, ChemCatChem 8 (2016) 21–33, https://doi.org/10.1002/cctc.201501269.

[15] G. Vilé, D. Albani, M. Nachtegaal, Z. Chen, D. Dontsova, M. Antonietti, N. López, J. Pérez-Ramírez, A Stable Single-Site Palladium Catalyst for Hydrogenations, Angew. Chem. Int. Ed. 54 (38) (2015) 11265–11269, https://doi.org/10.1002/anie.201505073.

[16] J.C. Liu, Y. Tang, Y.G. Wang, T. Zhang, J. Li, Theoretical Understanding of the Stability of Single-Atom Catalysts, Natl. Sci. Rev. 5 (2018) 638–641, https://doi.org/10.1093/nsr/nwy094.

[17] S. Schauermann, N. Nilius, S. Shaikhutdinov, H.-J. Freund, Nanoparticles for Heterogeneous Catalysis: New Mechanistic Insights, Acc. Chem. Res. 46 (8) (2013) 1673–1681, https://doi.org/10.1021/ar300225s.

[18] S. Mitchell, J. Pérez-Ramírez, Single Atom Catalysis: a Decade of Stunning Progress and the Promise for a Bright Future, Nat. Commun. 11 (2020) 1–3, https://doi.org/10.1038/s41467-020-18182-5.

[19] R. Lin, A.P. Amrute, J. Pérez-Ramírez, Halogen-Mediated Conversion of Hydrocarbons to Commodities, Chem. Rev. 117 (5) (2017) 4182–4247, https://doi.org/10.1021/acs.chemrev.6b00551.

[20] E. McFarland, Unconventional Chemistry for Unconventional Natural Gas, Science 338 (6105) (2012) 340–342, https://doi.org/10.1126/science:1226840.

[21] K. Ding, A.R. Derk, A. Zhang, Z. Hu, P. Stoimenov, G.D. Stucky, H. Metiu, E.W. McFarland, Hydrodebromination and Oligomerization of Dibromomethane, ACS Catal. 2 (4) (2012) 479–486, https://doi.org/10.1021/cs2006058.

[22] M.H. Nilsen, S. Svelle, S. Aravinthan, U. Olsbye, The Conversion of Chloromethane to Light Olefins over SAPO-34: The Influence of Dichloromethane Addition, Appl. Catal., A 367 (1-2) (2009) 23–31, https://doi.org/10.1016/j.apcata.2009.07.047.

[23] A.J. Saadun, S. Pablo-García, V. Paunović, Q. Li, A. Sabadell-Rendón, K. Kleemann, F. Krumeich, N. López, J. Pérez-Ramírez, Performance of Metal-Catalyzed Hydrodebromination of Dibromomethane Analyzed by Descriptors Derived from Statistical Learning, ACS Catal. 10 (11) (2020) 6129–6143, https://doi.org/10.1021/acscatal.0c00679.

[24] A.J. Saadun, S.K. Kaiser, A. Ruiz-Ferrando, S. Pablo-García, S. Büchele, E. Fako, N. López, J. Pérez-Ramírez, Nuclearity and Host Effects of Carbon-Supported Platinum Catalysts for Dibromomethane Hydrodebromination, Small 17 (16) (2021) 2005234, https://doi.org/10.1002/smll.202005234.

[25] A.J. Saadun, G. Zichittella, V. Paunović, B.A. Markaide-Aiastui, S. Mitchell, J. Pérez-Ramírez, Epitaxially Directed Iridium Nanostructures on Titanium Dioxide for the Selective Hydrodechlorination of Dichloromethane, ACS Catal. 10 (1) (2020) 528–542, https://doi.org/10.1021/acscatal.9b04467.

[26] J. Chastain, Handbook of X-ray Photoelectron Spectroscopy, Perkin-Elmer Corporation, Eden Prairie, 1992.

[27] S.K. Kaiser, R. Lin, F. Krumeich, O.V. Safonova, J. Pérez-Ramírez, Preserved in a Shell: High-Performance Graphene-Confined Ruthenium Nanoparticles in Acetylene Hydrochlorination, Angew. Chem. Int. Ed. 58 (35) (2019) 12297–12304, https://doi.org/10.1002/anie.201906916.

[28] J.J. Carberry, in: Catalysis: Science and Technology, Springer, Berlin, 1987, p. 131.

[29] D MEARS, Diagnostic Criteria for Heat Transport Limitations in Fixed Bed Reactors, J. Catal. 20 (2) (1971) 127–131, https://doi.org/10.1016/0021-9517(71)90073-X.

[30] G. Kresse, J. Furthmüller, Efficiency of Ab-Initio Total Energy Calculations for Metals and Semiconductors using a Plane-Wave basis Set, Comput. Mater. Sci. 6 (1) (1996) 15–50, https://doi.org/10.1016/0927-0256(96)00008-0.

[31] G. Kresse, J. Furthmüller, Efficient Iterative Schemes for Ab Initio Total-Energy Calculations using a Plane-Wave basis Set, Phys. Rev. B 54 (16) (1996) 11169–11186, https://doi.org/10.1103/PhysRevB.54.11169.

[32] J.P. Perdew, K. Burke, M. Ernzerhof, Generalized Gradient Approximation Made Simple, Phys. Rev. Lett. 77 (18) (1996) 3865–3868, https://doi.org/10.1103/PhysRevLett.77.3865.

[33] S. Grimme, J. Antony, S. Ehrlich, H. Krieg, A Consistent and Accurate Ab Initio Parametrization of Density Functional Dispersion Correction (DFT-D) for the 94 Elements H-Pu, J. Chem. Phys. 132 (15) (2010) 154104, https://doi.org/10.1063/1.3382344.

[34] P.E. Blöchl, Projector Augmented-Wave Method, Phys. Rev. B 50 (24) (1994) 17953–17979, https://doi.org/10.1103/PhysRevB.50.17953.

[35] G. Kresse, D. Joubert, From Ultrasoft Pseudopotentials to the Projector Augmented-Wave Method, Phys. Rev. B 59 (3) (1999) 1758–1775, https://doi.org/10.1103/PhysRevB.59.1758.

[36] G. Makov, M.C. Payne, Periodic Boundary Conditions in Ab Initio Calculations, Phys. Rev. B 51 (7) (1995) 4014–4022, https://doi.org/10.1103/PhysRevB.51.4014.

[37] G. Henkelman, B.P. Uberuaga, H. Jónsson, A Climbing Image Nudged Elastic Band Method for finding Saddle Points and Minimum Energy Paths, J. Chem. Phys. 113 (22) (2000) 9901–9904, https://doi.org/10.1063/1.1329672.

[38] G. Henkelman, H. Jónsson, Improved Tangent Estimate in the Nudged Elastic Band Method for finding Minimum Energy Paths and Saddle Points, J. Chem. Phys. 113 (22) (2000) 9978–9985, https://doi.org/10.1063/1.1323224.

[39] A. Heyden, A.T. Bell, F.J. Keil, Efficient Methods for finding Transition States in Chemical Reactions: Comparison of Improved Dimer Method and Partitioned Rational Function Optimization Method, J. Chem. Phys. 123 (22) (2005) 224101, https://doi.org/10.1063/1.2104507.

[40] G. Henkelman, H. Jónsson, A Dimer Method for finding Saddle Points on high Dimensional Potential Surfaces using only First Derivatives, J. Chem. Phys. 111 (15) (1999) 7010–7022, https://doi.org/10.1063/1.480097.

[41] M. Álvarez-Moreno, C. de Graaf, N. López, F. Maseras, J.M. Poblet, C. Bo, Managing the Computational Chemistry Big Data Problem: The ioChem-BD Platform, J. Chem. Inf. Model. 55 (2015) 95–103, https://doi.org/10.1021/ci500593j.

[42] A. Ruiz-Ferrando, CH_2X_2 Dataset, ioChem-BD database, 2021, https://doi.org/10.19061/iochem-bd-1-210.

[43] S.J. Freakley, J. Ruiz-Esquius, D.J. Morgan, The X-ray Photoelectron Spectra of Ir, IrO_2 and $IrCl_3$ revisited, Surf. Interface Anal. 49 (8) (2017) 794–799, https://doi.org/10.1002/sia.v49.810.1002/sia.6225.

[44] B.D. El-Issa, A. Katrib, R. Ghodsian, B.A. Salsa', S.H. Addassi, A Comparative Study of the Bonding in Different Halides of Iridium, Int. J. Quantum Chem. 33 (3) (1988) 195–216, https://doi.org/10.1002/(ISSN)1097-461X10.1002/qua.v33:310.1002/qua.560330305.

[45] David J. Morgan, Resolving Ruthenium: XPS Studies of Common Ruthenium Materials, Surf. Interface Anal. 47 (11) (2015) 1072–1079, https://doi.org/10.1002/sia.v47.1110.1002/sia.5852.

[46] M. Yu. Smirnov, A.V. Kalinkin, E.I. Vovk, V.I. Bukhtiyarov, Analysis of the Oxidation State of Platinum Particles in Supported Catalysts by Double Differentiation of XPS Lines, J. Struct. Chem. 57 (6) (2016) 1127–1133, https://doi.org/10.1134/S002247661606010X.